Noncoplanar and Counterrotating Incommensurate Magnetic Order Stabilized by Kitaev Interactions in γ-Li_{2}IrO_{3}

A. Biffin, R. D. Johnson, I. Kimchi, R. Morris, A. Bombardi, J. G. Analytis, A. Vishwanath, and R. Coldea

Non-Coplanar and Counter-Rotating Incommensurate Magnetic Order Stabilized by Kitaev Interactions in Stripyhoneycomb γ-Li$_2$IrO$_3$

A. Biffin[1], R. D. Johnson[1], I. Kimchi[2], R. Morris[1], A. Bombardi[3], J. G. Analytis[2,4], A. Vishwanath[2,4], and R. Coldea[1]

[1]*Clarendon Laboratory, University of Oxford, Parks Road, Oxford OX1 3PU, U.K.*
[2]*Department of Physics, University of California, Berkeley, California 94720. USA.*
[3]*Diamond Light Source Ltd., Didcot OX11 0DE, U.K. and*
[4]*Materials Science Division, Lawrence Berkeley National Laboratory, Berkeley, California 94720. USA.*

Materials that realize Kitaev spin models with bond-dependent anisotropic interactions have long been searched for, as the resulting frustration effects are predicted to stabilize novel forms of magnetic order or quantum spin liquids. Here we explore the magnetism of γ-Li$_2$IrO$_3$, which has the topology of a 3D Kitaev lattice of inter-connected Ir honeycombs. Using magnetic resonant x-ray diffraction we find a complex, yet highly-symmetric incommensurate magnetic structure with non-coplanar and counter-rotating Ir moments. We propose a minimal Kitaev-Heisenberg Hamiltonian that naturally accounts for all key features of the observed magnetic structure. Our results provide strong evidence that γ-Li$_2$IrO$_3$ realizes a spin Hamiltonian with dominant Kitaev interactions.

PACS numbers: 75.25.-j, 75.10.Jm

Magnetic materials with bond-dependent anisotropic interactions are candidates to display novel forms of magnetic order or quantum spin liquid states, as exemplified by the Kitaev model on the honeycomb lattice [1]. Here all spins interact via nearest-neighbor Ising exchanges, but a different Ising axis $(\mathsf{x},\mathsf{y},\mathsf{z})$ applies for the three different bonds emerging out of each lattice site. This leads to strong frustration effects that stabilize a novel gapless quantum spin liquid state with exotic excitations (Majorana fermions), which is exactly solvable in two dimensions. It was theoretically proposed [2] that such exotic Hamiltonians might be realized in magnetic materials containing edge-sharing cubic IrO$_6$ octahedra. The magnetic ground state of Ir^{4+} including the cubic crystal field and spin-orbit coupling is a spin-orbital doublet with $J_{\text{eff}} = 1/2$ [3], and super-exchange through the two 90° Ir-O-Ir paths is expected to lead to a dominant Ising interaction for the moment components normal to the Ir-O$_2$-Ir plane [2]. For a three-fold coordinated IrO$_6$ octahedron this leads to perpendicular Ising axes for the three nearest-neighbor bonds, as required for a Kitaev model. The 2D honeycomb-lattice α-Na$_2$IrO$_3$ [4–8] and α-Li$_2$IrO$_3$ [9, 10] are being intensively explored as candidate Kitaev materials, but as yet no clear evidence for novel Kitaev physics has been observed.

Generalizations of the Kitaev model to 3D lattices are also expected to have quantum spin liquid states [11–13]. The recently-synthesized structural polytypes "hyperhoneycomb" $\beta-$Li$_2$IrO$_3$ [14] and "stripyhoneycomb" $\gamma-$Li$_2$IrO$_3$ [15], which maintain the local three-fold coordination of edge-sharing IrO$_6$ octahedra, are prime candidates to display 3D Kitaev physics. To test for signatures of such physics we have performed magnetic resonant x-ray diffraction (MRXD) measurements [16] on single crystals of γ-Li$_2$IrO$_3$, scattering at the strong Ir L$_3$ resonance [5]. We have determined the complete magnetic structure for all 16 iridium sites in the unit cell, and

found an unexpectedly complex, yet highly symmetric magnetic structure comprised of non-coplanar, counter-rotating iridium magnetic moments located in zig-zag chains. Remarkably, the magnetic structure exhibits no net ferromagnetic or antiferromagnetic spin correlations, and as such one can rule out a model Hamiltonian whose primary ingredient is the nearest-neighbor Heisenberg interaction. Instead, motivated by the work of Jackeli and Khaliullin [17], and by arguments based on susceptibility anisotropy [13, 15], we present a minimal spin Hamiltonian with dominant Kitaev interactions that naturally reproduces all key features of the observed magnetic order. In particular, we point out that counter-rotation of moments on the zig-zag chains are naturally stabilized by Kitaev interactions. Our results therefore provide strong evidence that dominant Kitaev couplings govern the magnetism of γ-Li$_2$IrO$_3$.

The MRXD experiments were performed using the I16 beamline at Diamond (see [18] for details). Systematic searches along high-symmetry directions in reciprocal space revealed that at low temperatures new magnetic Bragg peaks appeared at satellite positions of reciprocal lattice points with an incommensurate propagation vector $\boldsymbol{q} = (0.57(1), 0, 0)$ [19]. The satellite peaks were found to be as sharp as structural peaks in all three reciprocal space directions, as illustrated for the $(0, 0, 16)+\boldsymbol{q}$ reflection in Fig. 1a); indicating coherent, 3D magnetic ordering. The peaks disappeared upon heating [Fig. 1(a), open circles] and the temperature-dependence of the intensity had a typical order parameter behavior [see Fig. 1(b)]. The absolute temperature values have been corrected for beam-heating effects through a calibration against specific heat measurements on the *same* sample, shown in Fig. 1(b) inset, which give $T_{\text{N}} = 39.5$ K.

The magnetic origin of the satellite reflections was further confirmed by analyzing the polarization of the scattered beam. Fig. 1(c) shows that the peak at $(0, 0, 16)+\boldsymbol{q}$
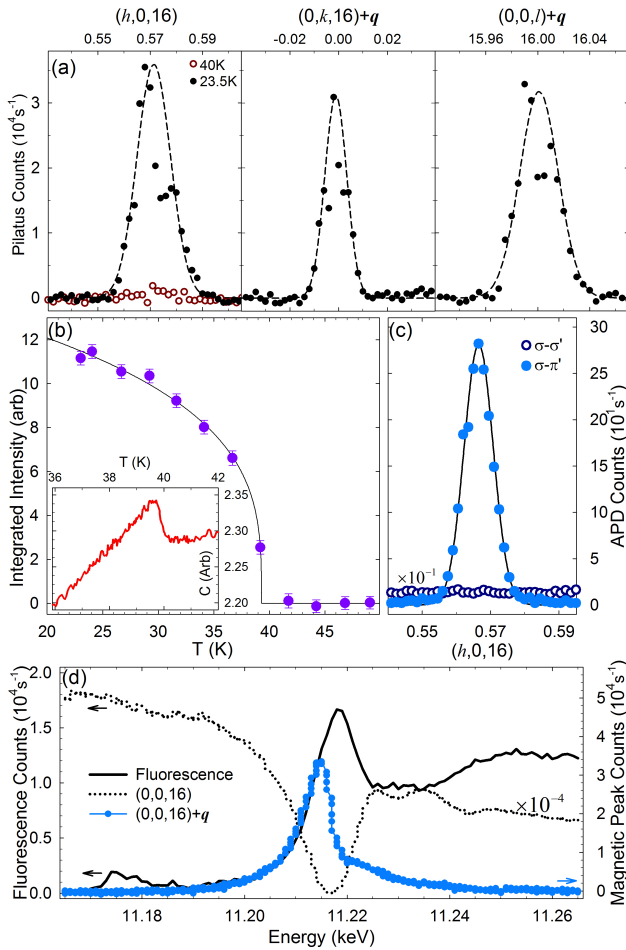
FIG. 1: (color online) Magnetic Bragg peak at $(0,0,16)+\boldsymbol{q}$. (a) Scans along orthogonal directions in reciprocal space (filled/open symbols at base temperature/above T_N). Dashed lines are fits to a Gaussian shape. (b) Temperature-dependence of the integrated magnetic peak intensity (solid line is guide to the eye, temperature values are corrected for beam heating effects, see text). Inset: specific heat data showing an anomaly at the onset of magnetic order. (c) Scans with a polarizer in the scattered beam: the magnetic signal is present only in the σ-π' channel (filled circles) and disappears in the σ-σ' (open circles) dominated by charge scattering (intensity scaled by 1/10). (d) Energy scan through the magnetic peak (blue squares) and a structural Bragg peak $(0,0,16)$ (dotted line, scaled by $1/10^4$), as well as the fluorescence scan (solid line).

FIG. 2: (color online) (a) Scan along the $(h,0,24)$ direction observing structural peaks at $h = 0,4$ (intensity scaled by $1/10^4$ for clarity), a multiple-scattering signal centered at $h = 2$, and magnetic peaks at $h = 0+q, 2 \pm q, 4-q$. Solid red line is the calculated magnetic scattering intensity [21] for the magnetic structure model depicted in Fig. 4. (b) $(h0l)$ reciprocal plane with filled circles, diamonds and red crosses indicating positions of structural peaks, measured magnetic peaks and the absence of peaks, respectively. Lattice points are also labelled by the magnetic basis vectors that have finite structure factor for magnetic peaks at satellite $\pm\boldsymbol{q}$ positions.

appeared only in the σ-π' channel (filled circles), and is absent in the σ-σ' channel (open circles), as expected for resonant diffraction that is of pure magnetic origin [16]. An energy scan performed whilst centered on the magnetic peak [Fig. 1(d)] showed a large resonant enhancement of the scattered intensity, again as expected for MRXD. The energy dependence is in stark contrast to that characteristic of a nearby structural peak (dotted line). Furthermore, the obtained resonance energy is similar to values found in other iridates [5, 20] and

agrees well with the edge of the measured fluorescence signal from the sample (solid line in Fig. 1(d)).

In total over 30 magnetic Bragg peaks were observed, and those measured in the $(h0l)$-plane are labelled in Fig. 2b). A representative scan along the $(h,0,24)$ direction is plotted in Fig. 2a), which shows strong structural Bragg peaks centered at $h = 0,4$, a multiple scattering signal centered at $h = 2$, and four magnetic Bragg peaks symmetrically displaced away from the above reflections. The scan illustrates the highly symmetric nature of the magnetic peak intensities and that $\boldsymbol{q}$ is distinctly different from the commensurate wavevector $(\frac{1}{2}00)$.

The magnetic iridium ions are located on two inequivalent sublattices in the orthorhombic unit cell, referred to as Ir and Ir', respectively (light and dark balls in Fig. 4). Each sublattice contains four sites in the primitive cell labelled 1 to 4 and $1'$ to $4'$, respectively. For a propagation vector $\boldsymbol{q} = (q,0,0)$ symmetry analysis [22] gives four types of magnetic basis vectors for $each$ of the two sublattices: $++++(F)$, $++--(C)$, $+--+(A)$ and $+-+-(G)$ where the $\pm$ signs denote a symmetry-imposed relation between the magnetic Fourier components at the sites

1-4 and 1′-4′.

Each of the four types of basis vectors has its own selection rules for a non-zero structure factor, so their presence can be directly confirmed from the observation of magnetic reflections at certain positions, and in some cases one can also identify the phase relation between the two sublattices. For example, all magnetic peaks along the $(h, 0, 24)$ line in Fig. 2a) can be uniquely assigned to scattering from F-type basis vectors. Satellites at $h = 0 + q$ and $4 - q$ arise from components that are equal in magnitude and in phase on the two sublattices, (F, F) in short-hand notation, whereas the satellites at $h = 2 \pm q$ originate from scattering by components equal in magnitude, but with opposite sign on the two sublattices, i.e. $(F, -F)$ (see [18] for details). The overall selection rules for magnetic scattering are illustrated in Fig. 2b). We have ruled out the presence of both C and G basis vectors as systematic searches (at 4 different azimuth angles) at the satellite positions $(0, 0, 23) + q$ and $(2, 0, 23) - q$ (red crosses) gave no sign of a magnetic signal. Furthermore, the observation of an AG magnetic peak at $(1, 1, 21) - q$, G being ruled out, confirms the presence of an A basis vector (azimuth scan in Fig. 3(a)).

The polarization dependence of the MRXD intensity allows a direct identification of the orientation of the magnetic moments. For a σ-polarized incident beam only the projection of the magnetic moments along the scattered beam direction, $\hat{\boldsymbol{k'}}$, contribute to the diffraction intensity [16]. By rotating the sample around the scattering vector $\boldsymbol{Q} = \boldsymbol{k'} - \boldsymbol{k}$ by the azimuth angle, Ψ, [see diagram in Fig.3a) inset] the projection of the magnetic moments onto $\hat{\boldsymbol{k'}}$ changes, giving a clear signature of the moment direction. We have measured the azimuth dependence for three magnetic peaks close to the sample surface normal, such that the Ψ rotation is almost around (001). The origin, $\Psi = 0$, is defined as when the (010) direction is in the scattering plane and pointing away from the source. Fig. 3a) shows the azimuth scan for a pure-A magnetic Bragg peak. The intensity drops to zero at $\Psi = 0$ and $180°$ and has maxima at $\pm 90°$, uniquely identifying that scattering comes from magnetic moment components along x (here x, y, z are along the orthorhombic a, b, c axes and scattering from y- and z-moment components, blue and green lines, respectively, have been calculated for comparison; hence identifying basis vector components in the combination $(A, \pm A)_x$, where the two sublattices are assumed to have equal magnitude moments. Similarly, the azimuth of the pure-F peak in Fig. 3b) originates from y-components antiparallel on the two sublattices, identifying the basis vector $(F, -F)_y$. Fig. 3c) shows the azimuthal dependence for a mixed FA peak, which uniquely identifies it as coming from basis vector components $\pi/2$ out-of-phase in the combination $i(A, -A)_x, (F, F)_z$. We note that this combination of relative phases between the x and z components on all the iridium sites is unique, where other com-
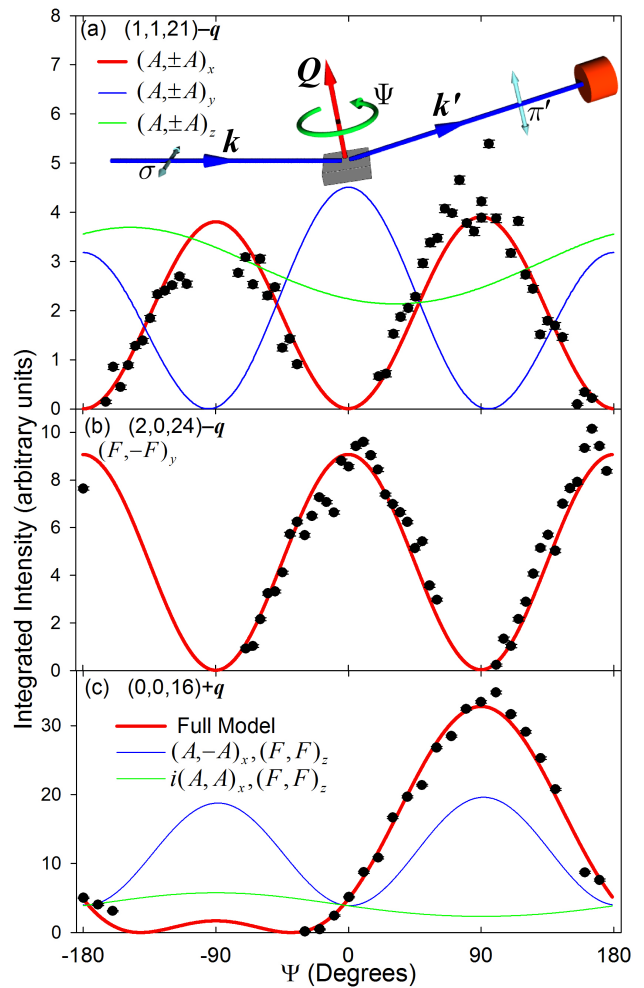
FIG. 3: (color online) Integrated intensity as a function of azimuth for three magnetic Bragg peaks, a) pure-A_x, b) pure-F_y and c) mixed-$F_z A_x$. Top diagram illustrates the scattering geometry. Data points (filled circles) are integrated peak intensities from rocking curve scans corrected for absorption and Lorentz factor. Thick (red) lines show fits that include all contributions to the MRXD structure factor [16, 21] from the magnetic structure model $i(A, -A)_x, -i(F, -F)_y, (F, F)_z$, depicted in Fig. 4. Blue/green curves in a,c) illustrate that other phase combinations of basis vectors are ruled out.

binations can be qualitatively ruled out (see blue/green curves in the same figure). The observed phase combination describes counter-rotating moments between consecutive sites along c (curly arrows in Fig. 4), which form counter-rotating zig-zag chains along a.

To determine the relative magnitudes of the magnetic moment components we performed a simultaneous fit to the magnetic scattering intensities in the three azimuth scans in Fig. 3 with four free parameters: the magnitudes of the moment amplitudes M_x and M_y relative to M_z, an overall intensity scale factor for the $(1, 1, 21) - q$ and $(2, 0, 24) - q$ peaks and a separate intensity scale factor for the $(0, 0, 16) + q$ peak (which was
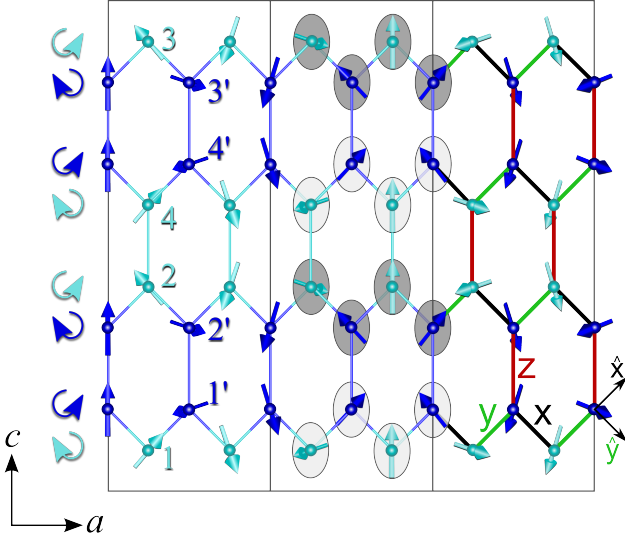
FIG. 4: (color online) Projection of the magnetic structure on the $(\boldsymbol{a}, \boldsymbol{c})$ plane showing 3 unit cells along the horizontal propagation direction a. Light and dark blue arrows show the moments on the Ir and Ir$'$ sublattices, with sites $1 - 4$ and $1' - 4'$, respectively. Curly arrows on the left side illustrate counter-rotating magnetic order between consecutive sites along c. In unit cell 2 light $(-\phi)$ and dark $(+\phi)$ shaded elliptical envelopes emphasize the confinement of the moments to alternate planes obtained from the (ac) plane by a rotation by $\mp\phi$ around c. In unit cell 3 color of bonds indicates the anisotropy axis of the Kitaev exchanges in (1), with $\eta = \mathsf{x}, \mathsf{y}, \mathsf{z}$ for black/green/red bonds, where $\hat{\mathsf{x}} = (\hat{\boldsymbol{a}} + \hat{\boldsymbol{c}})/\sqrt{2}$, $\hat{\mathsf{y}} = (\hat{\boldsymbol{a}} - \hat{\boldsymbol{c}})/\sqrt{2}$ and $\hat{\mathsf{z}} = \hat{\boldsymbol{b}}$ [15]).

measured on the same sample, but in a different experiment). The fit is shown by red solid lines in Fig. 3a-c), and gave values for the moment magnitude ratios $M_x : M_y : M_z = 0.65(4) : 0.58(1) : 1$. We note that this also quantitatively reproduces the observed ratio of the magnetic peak intensities in Fig. 2a) (red line).

Imposing the constraint of near-constant magnitude moment at every site requires the phase offset between the x and y components to be π or 0, giving the basis vector combination $i(A, -A)_x, i(-1)^m(F, -F)_y, (F, F)_z$, with $m = 1$ or 2. Both give similar structures and we plot in Fig. 4 the case $m = 1$. The moments are confined to rotate in one of two planes, obtained from the (ac) plane by rotation around the c-axis by an angle $\pm\phi$, with $\phi = \tan^{-1}\frac{M_y}{M_x} = 42(2)°$. The pattern is such that neighboring iridium zig-zag chains have alternate orientations of the moment rotation plane as indicated by the light and dark shaded envelopes in Fig. 4. The $m = 2$ case simply gives the opposite alternation of the rotation planes.

A key feature of the magnetic structure is the counter-rotation of neighboring moments. On two such sites, say 1 and $1'$, the spins projected to the ac-plane are $\boldsymbol{S}_{1,1'}(\boldsymbol{r}) = \hat{\boldsymbol{c}}\langle S^c\rangle \cos\boldsymbol{q}\cdot\boldsymbol{r} \pm \hat{\boldsymbol{a}}\langle S^a\rangle \sin\boldsymbol{q}\cdot\boldsymbol{r}$. We now rotate from the crystallographic a, b, c-axes to the Kitaev axes denoted by sans serif symbols $\mathsf{x}, \mathsf{y}, \mathsf{z}$ (see Fig. 4 cap-

tion) and consider the correlation between the S^{x} spin components $S_1^{\mathsf{x}} S_{1'}^{\mathsf{x}}$ across an x-type bond, or $S_1^{\mathsf{y}} S_{1'}^{\mathsf{y}}$ across a y-type bond. The net averaged correlation is finite, $\langle S_1^{\mathsf{x}} S_{1'}^{\mathsf{x}}\rangle_{\mathsf{x}} = \langle S_1^{\mathsf{y}} S_{1'}^{\mathsf{y}}\rangle_{\mathsf{y}} = \langle S^a\rangle\langle S^c\rangle\frac{1}{2}\sin\frac{\pi q}{2}$. We see that along each x-type bond the spins are aligned when they point along x, and anti-aligned when they point along y, and similarly for y-type bonds. Thus Kitaev interactions can stabilize the counter-rotating moments with a propagation vector $\boldsymbol{q}$ along $\boldsymbol{a}$. We therefore construct the following Kitaev-Heisenberg Hamiltonian as a minimal model

$$\mathcal{H} = \sum_{c-\mathrm{bonds}} \left[K_c S_i^{\eta_{ij}} S_j^{\eta_{ij}} + J_c \boldsymbol{S}_i \cdot \boldsymbol{S}_j + I_c^c S_i^c S_j^c \right] +$$
$$\sum_{d-\mathrm{bonds}} \left[K_d S_i^{\eta_{ij}} S_j^{\eta_{ij}} + J_d \boldsymbol{S}_i \cdot \boldsymbol{S}_j \right] + \sum_{2^{\mathrm{nd}} \langle\langle ij\rangle\rangle} J_2 \boldsymbol{S}_i \cdot \boldsymbol{S}_j \quad (1)$$

where interactions along the vertical (along c) bonds are denoted by the subscript c and interactions along the zig-zag (diagonal) bonds are denoted by the subscript d. K_c and K_d are the Kitaev interactions along c-bonds (of type $\eta_{ij} = \mathsf{z}$) and d-bonds (of type $\eta_{ij} = \mathsf{x}$ or y), respectively. To prevent $(0, 0, q_c)$ instabilities we have introduced an Ising coupling I_c^c of the S^c spin components, and finally a Heisenberg coupling J_2 between second nearest neighbors. We take the following values for the parameters (in units of meV): $K_c = -15, K_d = -12, J_c = 5, J_d = 2.5, I_c^c = -4.5, J_2 = -0.9$ [18], where the overall scale was set such as to have the calculated ordering transition temperature agree with the experimental value.

The Hamiltonian was analyzed in Fourier space using the Luttinger-Tisza approximation [18]. This gave the lowest-energy mode identical to the (S^a, S^c) coplanar projection of the magnetic structure in Fig. 4 with $\langle S^c\rangle > \langle S^a\rangle$. To obtain fixed-length spins requires mixing with another mode, and the lowest energy mode available at the same wavevector has collinear order of the S^b components with a pattern such that the mixed mode exactly reproduce the observed non-coplanar structure. Furthermore, the S^b components are co-aligned along all the c-axis bonds, and hence stabilized by the large FM K_c Kitaev exchange. The mixing amplitude, related to the tilt angle ϕ, is fixed for unit length spins, but changes continuously with the Hamiltonian parameters. Decreasing the strength of the Kitaev interactions prevents the ground state from producing unit-length spins through this mixing mechanism, and importantly, we find that the non-coplanar tilt angle observed in γ-Li$_2$IrO$_3$ requires relatively large Kitaev exchanges within the minimal model.

To summarize, through MRXD measurements on γ-Li$_2$IrO$_3$ single crystals we have observed an incommensurate, non-coplanar magnetic structure with counter-rotating moments. A Kitaev-Heisenberg Hamiltonian can fully explain the observed complex magnetic structure, providing strong evidence that γ-Li$_2$IrO$_3$ is an experimental realization of 3D Kitaev physics in the solid

state.

---

[1] A. Kitaev, Ann. Phys. (N.Y.) **321**, 2 (2006).

[2] J. Chaloupka, G. Jackeli and G. Khaliullin, Phys. Rev. Lett. **105**, 027204 (2010).

[3] B. J. Kim, H. Ohsumi, T. Komesu, S. Sakai, T. Morita, H. Takagi, T. Arima, Science **323**, 1329 (2009).

[4] Y. Singh, P. Gegenwart, Phys. Rev. B **82**, 064412 (2010).

[5] X. Liu, T. Berlijn, W.-G. Yin, W. Ku, A. M. Tsvelik, Young-June Kim, H. Gretarsson, Yogesh Singh, P. Gegenwart, and J. P. Hill, Phys. Rev. B **83**, 220403(R) (2011).

[6] S. K. Choi, R. Coldea, A. N. Kolmogorov, T. Lancaster, I. I. Mazin, S. J. Blundell, P. G. Radaelli, Yogesh Singh, P. Gegenwart, K. R. Choi, S.-W. Cheong, P. J. Baker, C. Stock, and J. Taylor, Phys. Rev. Lett. **108**, 127204 (2012).

[7] F. Ye, S. Chi, H. Cao, B. C. Chakoumakos, J. A. Fernandez-Baca, R. Custelcean, T. F. Qi, O. B. Korneta, and G. Cao, Phys. Rev. B **85**, 180403(R) (2012).

[8] H. Gretarsson, J. P. Clancy, Y. Singh, P. Gegenwart, J. P. Hill, J. Kim, M. H. Upton, A. H. Said, D. Casa, T. Gog, and Y.-J. Kim, Phys. Rev. B **87**, 220407(R) (2013).

[9] M. J. O'Malley, H. Verweij and P.M. Woodward, J. Solid State Chem. **181**, 1803 (2008).

[10] Y. Singh, S. Manni, J. Reuther, T. Berlijn, R. Thomale, W. Ku, S. Trebst, and P. Gegenwart, Phys. Rev. Lett. **108**, 127203 (2012).

[11] S. Mandal and N. Surendran, Phys. Rev. B **79**, 024426 (2009).

[12] Eric Kin-Ho Lee, R. Schaffer, S. Bhattacharjee, and Y. B. Kim, Phys. Rev. B **89**, 045117 (2014).

[13] I. Kimchi, J. G. Analytis, A. Vishwanath, arXiv:1309.1171 (2013).

[14] T. Takayama, A. Kato, R. Dinnebier, J. Nuss, H. Takagi, arXiv.org/1403.3296 (2014).

[15] K. A. Modic, T. E. Smidt, I. Kimchi, N. P. Breznay, A. Biffin, S. Choi, R. D. Johnson, R. Coldea, P. Watkins-Curry, G. T. McCandless, J. Y. Chan, F. Gandara, Z. Islam, A. Vishwanath, A. Shekhter, R. D. McDonald, and J. G. Analytis, Nature Comm **5**, 4203 (2014).

[16] J. P. Hill and D. F. McMorrow, Acta Cryst. A **52**, 236, (1996).

[17] G. Jackeli and G. Khaliullin, Phys. Rev. Lett. **102**, 017205 (2009)

[18] Supplemental material

[19] The uncertainty in the value of q is estimated from combining uncertainties in the crystal orientation (UB-matrix) and the I16 instrument intrinsic sphere of uncertainty.

[20] S. Boseggia, R. Springell, H. C. Walker, H. M. Rønnow, Ch. Rüegg, H. Okabe, M. Isobe, R. S. Perry, S. P. Collins, and D. F. McMorrow, Phys. Rev. Lett. **110**, 117207 (2013).

[21] http://forge.ill.eu/svn/magnetix

[22] *BasiReps* software part of the *FullProf* suite, J. Rodriguez-Carvajal, Physica B **192**, 55 (1993).